PNAS RESEARCH ARTICLE | ENGINEERING

Active learning design of bcc solid solution alloys with gigapascal strength and elemental metal–level ductility

Zhixing Wang[a,1], Xiangyue Chen[b,1], Dongqing Zhang[a,1], Ge Wu[a], Yan Ma[c], Xiaoqin Zeng[b], Ziyuan Rao[b,2], Chang Liu[a,2], and Evan Ma[a]

Edited by David Weitz, Harvard University, Cambridge, MA; received October 28, 2025; accepted December 21, 2025

Body-centered cubic (bcc) alloys can achieve gigapascal-level yield strengths but typically are limited in tensile ductility (<20%), contrasting sharply with elemental metals (the largest elongation of ~50%). Multi-principal-element alloys offer vast compositional space to reach synergistic strength–ductility combinations. However, combinatorial trial-and-error exploration is prohibitively costly, while machine learning (ML) approaches are hindered by data scarcity. Here, we develop an ML-guided framework integrating active learning with physics-informed Bayesian optimization to rapidly converge on optimal compositions. The resulting $Ti_{36}V_{14}Nb_{22}Hf_{22}Zr_1Al_5$ alloy achieves a yield strength of 953 MPa and a large tensile ductility of 42%. The high strength arises from the substantial lattice distortion, as well as the ~1-nm-sized local chemical fluctuations (LCFs) inherent to the highly concentrated bcc solid solution. The ubiquitous LCFs also substantially promote dislocation multiplication and strain hardening, enabling a large tensile ductility. Our approach demonstrates ML's efficacy in accelerating the finding of high-performance alloys.

multi-principal-element alloys | machine learning | strength | ductility

Significance

This work successfully accelerated the finding of multi-principal-element alloys (MPEAs) by integrating active learning with physical parameters, leading to the identification of a $Ti_{36}V_{14}Nb_{22}Hf_{22}Zr_1Al_5$ alloy with exceptional properties. The coupling between nanoscale compositional fluctuations and lattice distortion serves as the fundamental mechanism for the alloy's stable strain hardening behavior. This breakthrough overcomes the limited ductility in traditional body-centered cubic (bcc) alloys caused by planar dislocation slip. This research establishes an innovative framework for alloy design and introduces a pathway to promote the strength–ductility synergy of MPEAs.

Scientists have long been pursuing high-strength metals with large ductility. Yet, strengthening strategies such as grain boundary hardening or precipitation hardening often compromise ductility (1). Body-centered cubic (bcc) alloys with gigapascal strength are plagued by another issue: They are prone to planar slip behavior, which concentrates dislocations into localized bands, rendering unstable plastic flow at strains below 20%—a stark contrast to their constituent elemental metals (2, 3) (largest elongation of ~50%).

Recent developments in bcc multi-principal-element alloys (MPEAs) demonstrate excellent mechanical properties (4). For instance, a $Ti_{50}Zr_{18}Nb_{15}V_{12}Al_5$ (at%) alloy with B2-like local chemical order (LCO) (5) and a $HfNbTiVAl_{10}$ (at%) alloy featuring hierarchical chemical fluctuations including spinodally modulated composition waves (6) have achieved both high strength and large ductility. However, it is unknown if a uniform MPEA solid solution, one that contains no observable LCOs, which themselves could instigate planar slip bands (localized deformation as mentioned earlier), nor 10-nm scale composition waves, whose development relied on complex thermodynamic/kinetic conditions for controlled spinodal decomposition, can also reach strength–ductility properties similar to the best bcc MPEAs thus far (5, 6). Such an extreme of single-phase solid solutions may be possible, but current alloy design paradigms relying on empirical trial-and-error approaches face prohibitive costs when navigating the vast compositional space of MPEAs, spanning $>10^{20}$ possible compositions for quinary systems.

An approach to rapidly screen the composition–property relationship is urgently needed. Machine learning (ML) methods show high potential to significantly reduce the development costs (7). However, prevailing data-driven approaches often suffer from limited extrapolative ability beyond the training dataset, high demand for labeled data, and insufficient integration of physical metallurgy principles, hindering their reliability and efficiency (8, 9). Here, we establish an active learning loop, coupled with physics-informed Bayesian optimization framework, to accelerate the finding of optimal MPEAs. We then integrate three critical principles into the Bayesian optimization framework to focus on the desirable structure–composition regime. Specifically, the parameters for screening include i) lattice distortion as a metric governing dislocation motion pattern, ii) atom-level descriptors (e.g., electronegativity, atomic radius) modulating enthalpic interaction, and iii) phase stability criteria ensuring a single-phase bcc structure. This strategic fusion of active learning with domain knowledge finds a $Ti_{36}V_{14}Nb_{22}Hf_{22}Zr_1Al_5$ solid solution with a high yield strength of 953 MPa and a large tensile ductility (42%) on par with elemental bcc metals, which is an outstanding combination among bcc solid solution alloys.

Author affiliations: [a]Center for Alloy Innovation and Design, Center for Advancing Materials Performance from the Nanoscale and Hysitron Applied Research Center in China, State Key Laboratory for Mechanical Behavior of Materials, School of Materials Science and Engineering, Xi'an Jiaotong University, Xi'an 710049, China; [b]National Engineering Research Center of Light Alloy Net Forming, School of Materials Science and Engineering, Shanghai Jiao Tong University, Shanghai 200240, China; and [c]Department of Materials Science and Engineering, Delft University of Technology, Delft NL-2628 CD, Netherlands

Author contributions: Z.R., C.L., and E.M. designed research; Z.W., X.C., D.Z., G.W., and X.Z performed research; X.C., D.Z., and Y.M. contributed new reagents/analytic tools; Z.W., Z.R., and C.L. analyzed data; and Z.W., C.L., and E.M. wrote the paper.

The authors declare no competing interest.

This article is a PNAS Direct Submission.

[1]Z.W., X.C., and D.Z. contributed equally to this work.

[2]To whom correspondence may be addressed. Email: ziyuanrao@sjtu.edu.cn or chang.liu@xjtu.edu.cn.

This article contains supporting information online at https://www.pnas.org/lookup/suppl/doi:10.1073/pnas.2530922123/-/DCSupplemental.

Published January 29, 2026.

In terms of microstructure evolution, TEM analysis reveals uniform storage of massive amounts of dislocations in samples after deformation, rather than localized planar slip bands as in previous gigapascal-strength bcc MPEAs. Such an unusual pattern of dislocation proliferation promotes strain hardening and strain delocalization. Our data-driven methodology combined with physics-guided exploration demonstrates significant acceleration in alloy development, compared to the conventional "trial and error" approaches.

Results and Discussion

Fig. 1 schematically presents the physics-informed active learning loop, which integrates domain knowledge with data-driven optimization for designing advanced MPEAs (the detailed ML methods are described in the *SI Appendix, Text*). A mechanical properties database (with 111 datapoints taken from 45 literatures) comprising multidimensional features was built (*SI Appendix*, Fig. S1). These features include composition, heat treatment, and physical parameters selected by a three-stage feature screening approach (*SI Appendix*, Figs. S2 and S3). We then utilized active learning with bootstrap resampling for uncertainty quantification, training 1,000 models on randomly resampled datasets. Through rigorous cross-validation and Bayesian hyperparameter tuning, the support vector regression (SVR) model with optimal accuracy for both yield strength and elongation (*SI Appendix*, Figs. S4 and S5) was chosen. Alloy candidates are generated by Bayesian optimization via the Multi-Objective Upper Confidence Bound (MO-UCB) acquisition function to balance exploration and exploitation. Efficient global optimization (EGO) is used to avoid local optima. We then prioritize the top three candidates with high strength and ductility, within the compositional space that is set with the help of domain knowledge (*SI Appendix*, Fig. S6).

Lattice distortion is a critical feature governing the yield strength of bcc MPEAs (10). Enhanced lattice strain fields, arising from severe atomic size mismatch between constituent elements, could amplify solid-solution strengthening effects (11). Guided by this mechanistic understanding, the Ti–V–Nb–Hf system was designed, particularly leveraging the pronounced atomic size difference between V (1.316 Å) and Hf (1.578 Å) to induce nonuniform lattice strains. In addition, Zr with an exceptionally large atomic radius (1.603 Å) was considered for an enhanced solid-solution strengthening effect. Al was further introduced, capitalizing on its negative mixing enthalpy with the other constituent elements to strengthen the interatomic bonding (6). Mo and Ta are not included for consideration since their high melting points (>2,500 °C) would bring difficulty to ensure adequate mixing in the cast alloy. In this study, we constrain the compositions in a range that forms single-phase solid solutions (12), as the latter often exhibit a higher ductility compared to their multiphase counterparts (13). The criteria to be satisfied are $0 \le \delta \le 8.5$, $-22 \le \Delta H_{mix} \le 7$ kJ/mol, $11 \le \Delta S_{mix} \le 19.5$ J/(K·mol), and the

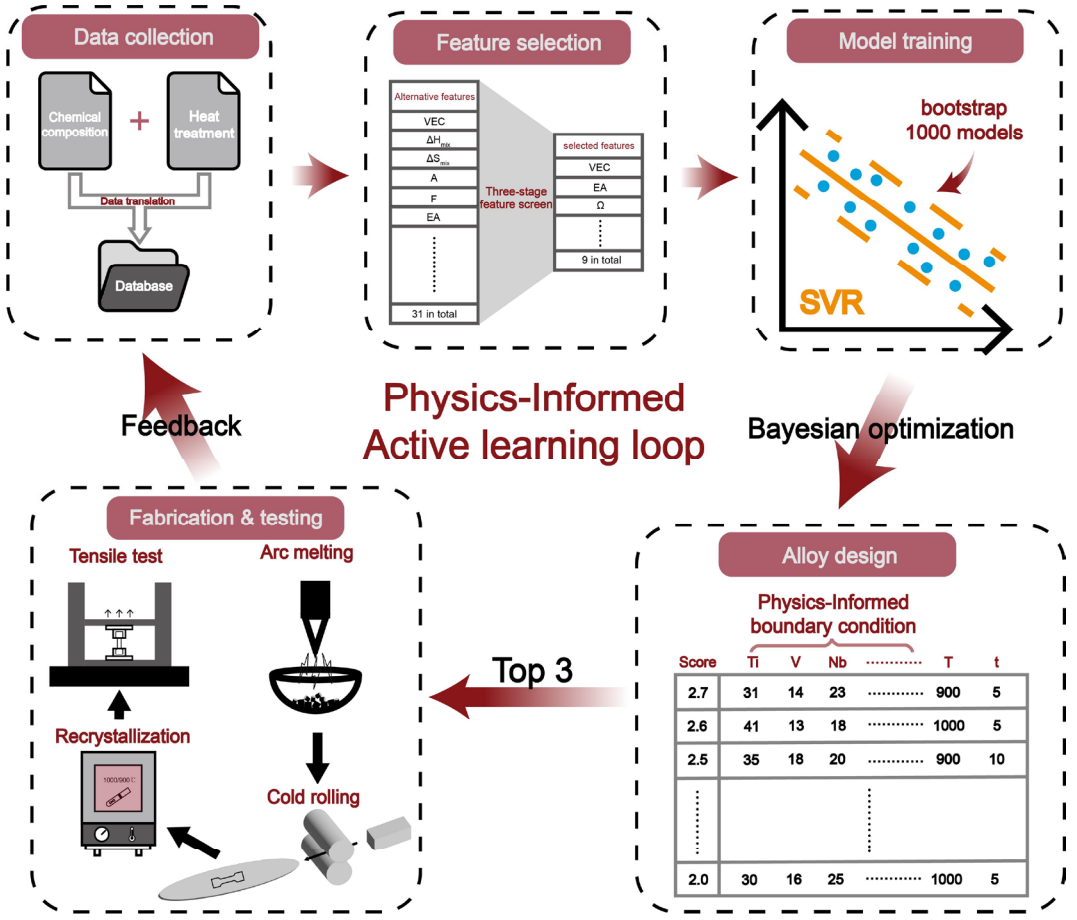

Fig. 1. Machine learning framework for iterative search of strong and ductile BCC MPEAs. Our strategy begins with data collection. Next, the three-stage feature screening approach is used to screen out the most effective feature combinations. Subsequently, a total of 1,000 SVR (support vector regression) models were trained on randomly resampled datasets with replacement (referred to as Bootstrap resampling). Alloy candidates are then generated via Bayesian optimization within the given physical-based boundary condition and ranked by the Multi-Objective Upper Confidence Bound (MO-UCB) acquisition function: $YS(\mu+\kappa\cdot\sigma)\times EL(\mu+\kappa\cdot\sigma)$. The top three candidates are fabricated and tested. The obtained mechanical performance data are fed back into the model, enabling continuous improvement of model performance through this iterative cycle.

calculation details for δ, ΔH_{mix}, and ΔS_{mix} are given in *SI Appendix, Text*. Also, the Zr addition was limited to low concentrations so as to avoid brittle Laves phase (14) or B2-like LCO (5). Leveraging such physical insights, appropriate boundary conditions were defined for the ML-generated alloy compositions, to ensure the formation of desired structures (*SI Appendix*, Table S3). The ML-predicted alloys were produced and processed, and the experimentally measured mechanical properties were then used to train the ML models. Experimental validation of alloys feedback created a self-improving loop, demonstrating how integration of machine learning accelerates the finding of high-performance materials.

With only four iterations, the active learning landed a $Ti_{36}V_{14}Nb_{22}Hf_{22}Zr_1Al_5$ alloy with high strength and ductility (*SI Appendix*, Tables S4 and S5). For comparison, we prepared a $Ti_{38}V_{15}Nb_{23}Hf_{24}$ base alloy, without alloying with Zr and Al, as a reference bcc solid solution. Electron backscattered diffraction (EBSD) and X-ray diffraction (XRD) analysis confirm that after Zr and Al coalloying, the $Ti_{36}V_{14}Nb_{22}Hf_{22}Zr_1Al_5$ alloy remains the desired single-phase bcc structure (Fig. 2*A*). The $Ti_{36}V_{14}Nb_{22}Hf_{22}Zr_1Al_5$ and the $Ti_{38}V_{15}Nb_{23}Hf_{24}$ base alloy have comparable grain sizes of 63.18 μm and 64.88 μm (Fig. 2*A* and *SI Appendix*, Fig. S7).

We further investigated the nanoscale and atomic-scale elemental distribution of the $Ti_{36}V_{14}Nb_{22}Hf_{22}Zr_1Al_5$ alloy by using high-angle annular dark-field (HAADF) imaging and energy-dispersive X-ray spectroscopy (EDS). Fig. 2 *B* and *C* present the HAADF image and the corresponding EDS maps of individual constituent elements of the $Ti_{36}V_{14}Nb_{22}Hf_{22}Zr_1Al_5$ alloy. The EDS signal intensity in the map for any elemental species represents the local mass (density of the atoms) (15). For the EDS maps in Fig. 2*C*, all the elements share a similar degree of homogeneity, suggesting that the elements are distributed homogeneously at the nanometer scale. At the atomic level, interestingly, EDS maps and the corresponding line profiles (Fig. 2 *E* and *F*) show enrichment or depletion of various elements in altering Nb-enriched and (Ti, Hf)-enriched regions, which have a spatial size scale of ~1 nm (*SI Appendix*, Fig. S8). Nb exhibits an inverse correlation in the spatial distribution with Hf and Ti (Fig. 2*E*). This trend can be explained by a positive mixing enthalpy (ΔH_{mix}) between Nb and Hf (4 kJ/mol), Nb and Ti (2 kJ/mol) (16). Note that Zr and Al distribute uniformly across. Such local chemical fluctuations (LCFs) have been observed before in many MPEA solutions (15, 17) and can be understood in the following way. While there are no observable LCOs under TEM, MPEA solid solutions almost always (few exceptions) develop LCFs, because such highly concentrated solutions are prone to appreciable composition fluctuation on ~1 nm scale (18). Part of this fluctuation is statistical, which would be visible even in an ideal solution when the concentration of the alloying element is high (18). In the meantime, in most systems, the composition fluctuation is chemically amplified, with some degree of short-range chemical order/segregation driven by the negative/positive enthalpy of mixing. The 1-nm length alternating regions (atomic columns) of compositional enrichment/depletion, as seen in Fig. 2*E*, are expected to show an appreciable chemical order parameter, if it can be evaluated for local regions (19). This is particularly the case when the solution mixes constituent species that are quite dissimilar, which is the case in our alloy: The Al–Ti, Al–Hf, and Zr–Al pairs are known to have rather large negative mixing enthalpy (*SI Appendix*, Table S6), indicating highly attractive/preferential bonding between them. The ubiquitously present LCFs, although not as effective as precipitates or (TEM-visible) LCOs, would still retard dislocation motion (note that they would not induce stress concentration like precipitated dispersions). Furthermore, the relatively large atomic size difference between Zr (1.603 Å) (12) and the other constituent atoms enhances lattice distortions. Geometric phase analyses (GPA) (*Inset* in Fig. 2*D*) of the

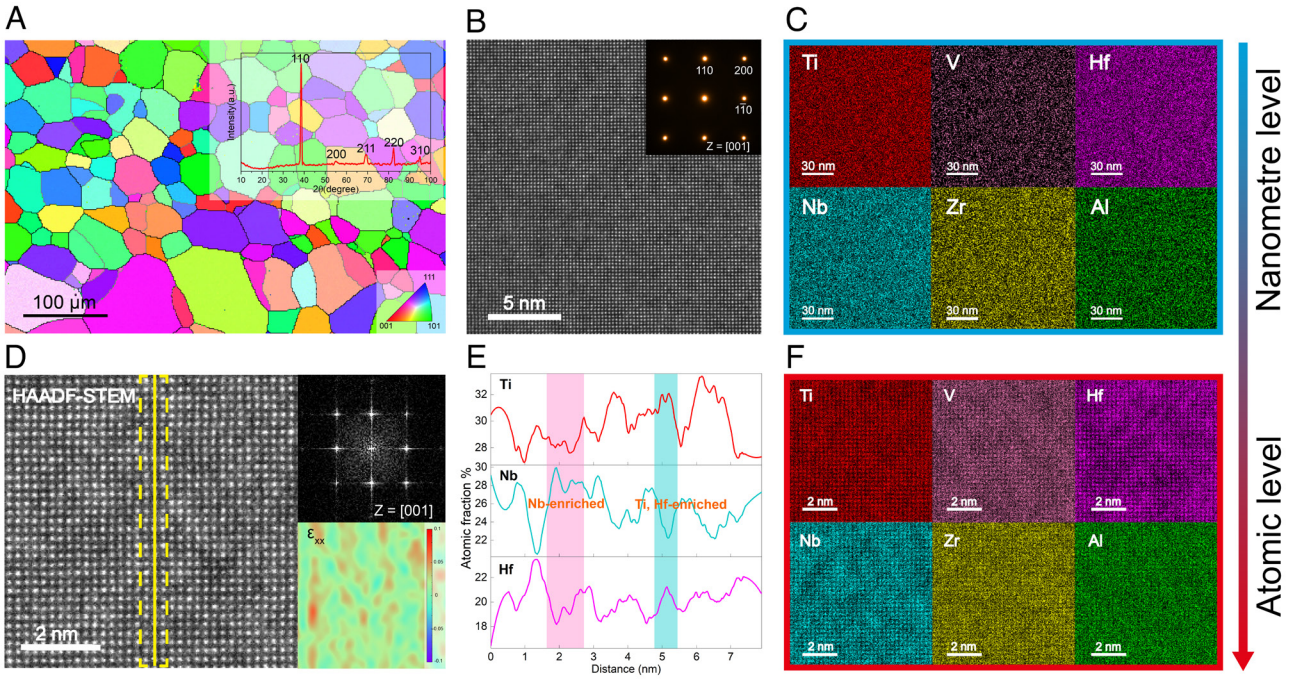

Fig. 2. Structure and composition of the $Ti_{36}V_{14}Nb_{22}Hf_{22}Zr_1Al_5$ alloy. (*A*) EBSD inverse pole figure map of the alloy, the *Inset* is the XRD pattern. The $Ti_{36}V_{14}Nb_{22}Hf_{22}Zr_1Al_5$ alloy adopts a single-phase bcc structure. (*B*) HAADF-STEM image of the lattice, the *Inset* is a SAED pattern. (*C*) EDS maps of the constituent elements at nanometer level. (*D*) Atom-resolved HAADF-STEM image taken along the [001] zone axis. The *Bottom-Right Inset* shows the corresponding atomic strain ε_{xx} map, derived from the lattice image using geometric phase analysis (GPA). The *Top-Right Inset* is the corresponding FFT pattern. (*E*) Line profiles of atomic fractions of individual elements in the yellow dashed box in (*D*). (*F*) EDS maps of the region in (*D*), showing ~1-nm sized Nb-enriched and Ti, Hf-enriched regions.

atom-resolved STEM image reveal alternating distribution of positive and negative localized strain, coinciding with the alternating 1-nm LCFs (6). For such an MPEA solid solution, there would be a rugged atomic as well as energy landscape for the dislocations moving through the lattice (20). This constitutes a major difference from traditional solid solutions, justifying our search targeting high strength/ductility using multi-principal-element solid solutions.

Next, we show that the alloy designed via the present ML framework achieves superior mechanical properties. Fig. 3 displays the tensile engineering stress–strain curves of the $Ti_{36}V_{14}Nb_{22}Hf_{22}Zr_1Al_5$ and the $Ti_{38}V_{15}Nb_{23}Hf_{24}$ base alloy. The Zr/Al coalloying leads to a substantial improvement in strength and ductility. Specifically, the yield strength (σ_y) increases from 800 MPa to 953 MPa, and the tensile ductility (ε_f) is elevated from 30 to 42%. Large dimples are observed in the fractured surface of the $Ti_{36}V_{14}Nb_{22}Hf_{22}Zr_1Al_5$ alloy (*SI Appendix*, Fig. S9), confirming its ductile nature. The true stress–strain curve (*Inset* in Fig. 3*A*) shows that the $Ti_{36}V_{14}Nb_{22}Hf_{22}Zr_1Al_5$ alloy sustains a high true stress level of ~1.2 GPa. The synergy between strength and tensile ductility achieved via Zr/Al coalloying is outstanding among the state-of-the-art bcc substitutional solid-solution MPEAs (Fig. 3*B*), showcasing what ML-aided design can achieve for high-performance alloys (21, 22). While strengthening often comes at the expense of ductility, the $Ti_{36}V_{14}Nb_{22}Hf_{22}Zr_1Al_5$ alloy exhibits a gigapascal-level strength and a high tensile ductility (42%) on par with those of the constituent elemental metals (largest elongation of ~50%) (2, 3). Such a combination of strength–ductility is impressive.

The $Ti_{36}V_{14}Nb_{22}Hf_{22}Zr_1Al_5$ alloy exhibits a strength increase of 153 MPa compared to the $Ti_{38}V_{15}Nb_{23}Hf_{24}$ base alloy. These two alloys have comparable grain size (*SI Appendix*, Fig. S7), indicating that the strength gain is not due to grain refinement. As mentioned earlier, the Nb-enriched and (Ti, Hf)-enriched 1 nm-scale regions show undulating lattice strains (Fig. 2*D*, resulting in a rugged landscape for dislocation to navigate through. This is because the Zr has a markedly different atomic radius from the matrix elements, such that the localized distortion of the lattice planes is substantially enhanced when Zr is added, increasing the difficulty for dislocation motion. Moreover, the Zr-Al, Hf-Al, and Ti-Al pairs have a large negative mixing enthalpy of −44 kJ/mol, −39 kJ/mol, and −30 kJ/mol (16), respectively, which is an order of magnitude more negative than that between the other elements (ranging from −4 kJ/mol to 4 kJ/mol). The increased bonding/affinity between elements promotes LCFs, resulting in an improved strength, as discussed in ref. 35. Then, in this MPEA, which is more complex than a traditional solid solution, the traversing dislocations require additional driving force to move across the lattice comprised of rather different atomic species (especially Zr and Al) and 1 nm-scale LCFs. The yield strength of the alloy is elevated as a result, explaining the observed yield strength approaching 1 GPa.

In what follows, we illustrate the underlying mechanisms for the remarkable tensile ductility of the $Ti_{36}V_{14}Nb_{22}Hf_{22}Zr_1Al_5$ alloy despite the gigapascal-level yield strength. TEM analysis (Fig. 4) suggests that the alloy remains a bcc structure upon deformation, with no sign of phase transformation or twining. The $Ti_{36}V_{14}Nb_{22}Hf_{22}Zr_1Al_5$ alloy deforms via the glide of dislocations. In high-strength bcc alloys, dislocations are often highly confined in narrow slip bands, resulting in strain localization and early fracture (36, 37). Distinctly different dislocation slip and interaction behavior is observed in the $Ti_{36}V_{14}Nb_{22}Hf_{22}Zr_1Al_5$ alloy. At a strain of 5%, abundant wavy dislocations are uniformly distributed throughout the deforming volume, with no planar slip band observed (Fig. 4*A*). Furthermore, the dislocation lines are smooth and curved. This morphology contrasts with what was observed in previous high-strength bcc alloys, in which edge dislocations rapidly glide away (38), leaving behind rectilinear dislocations dominated by screw orientations. The large lattice distortion in the $Ti_{36}V_{14}Nb_{22}Hf_{22}Zr_1Al_5$ alloy could promote preexisting kinks on screw dislocations and increase the local trapping for edge dislocations (39). This retains edge components and enables the edge and screw segments of a dislocation to have comparable velocities (40). As such, the normally large disparity between the motion of edge and screw dislocations in bcc metals would be diminished (39). The coupled motion of edge and screw dislocations has been taken as an indicator for the efficiency of Frank-Read dislocation sources, and of the activation of high-order slip systems (41). The resultant dislocation proliferation leads to a relatively uniform distribution of a high-density of dislocations, without their concentration into a narrow planar-slip band at an early stage of deformation.

The wavy dislocation morphology and nonlocalized distribution of dislocations bode well for strain hardening and strain delocalization. This is demonstrated in Fig. 4*B*, at 10% strain: Slip

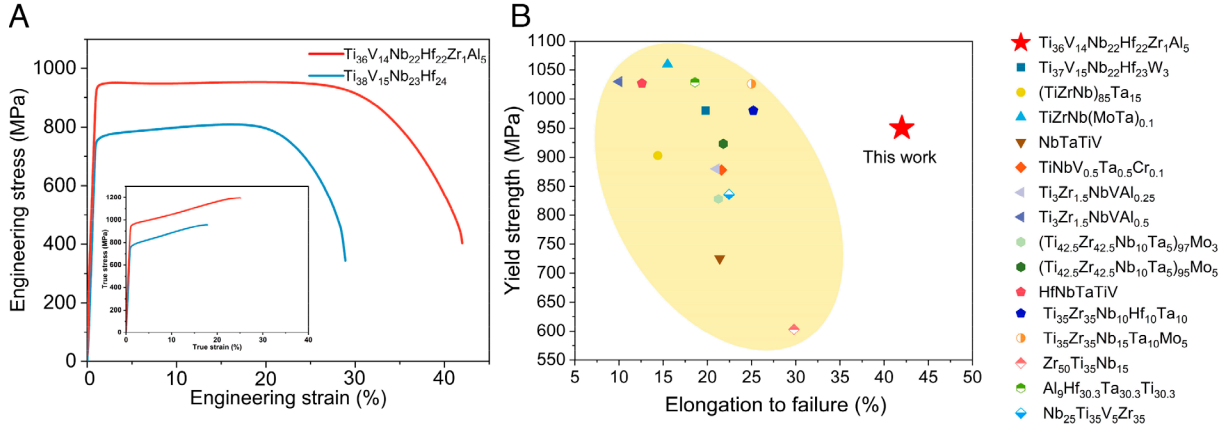

Fig. 3. Tensile properties of $Ti_{36}V_{14}Nb_{22}Hf_{22}Zr_1Al_5$ alloy and the base alloy at ambient temperature. (*A*) Engineering tensile stress–strain curves and true stress–strain curves (*Inset*, the segment after the engineering stress peaks was excluded from the calculation, as it is beyond the uniform deformation regime) of the $Ti_{36}V_{14}Nb_{22}Hf_{22}Zr_1Al_5$ alloy and the base alloy. (*B*) A comparison of yield strength and elongation to failure with the state-of-the-art substitutional single-phase bcc MPEAs, including $Ti_{37}V_{15}Nb_{22}Hf_{23}W_3$ (23), $(TiZrNb)_{85}Ta_{15}$ (24), $TiZrNb(MoTa)_{0.1}$ (25), NbTaTiV (3), $TiNbV_{0.5}Ta_{0.5}Cr_{0.1}$ (26), $Ti_3Zr_{1.5}NbVAl_{0.25}$ (27), $Ti_3Zr_{1.5}NbVAl_{0.5}$ (27), $(Ti_{42.5}Zr_{42.5}Nb_{10}Ta_5)_{97}Mo_3$ (28), $(Ti_{42.5}Zr_{42.5}Nb_{10}Ta_5)_{95}Mo_5$ (28), HfNbTaTiV (29), $Ti_{35}Zr_{35}Nb_{10}Hf_{10}Ta_{10}$ (30), $Ti_{35}Zr_{35}Nb_{15}Ta_{10}Mo_5$ (31), $Zr_{50}Ti_{35}Nb_{15}$ (32), $Al_9Hf_{30.3}Ta_{30.3}Ti_{30.3}$ (33), and $Nb_{25}Ti_{35}V_5Zr_{35}$ (34).

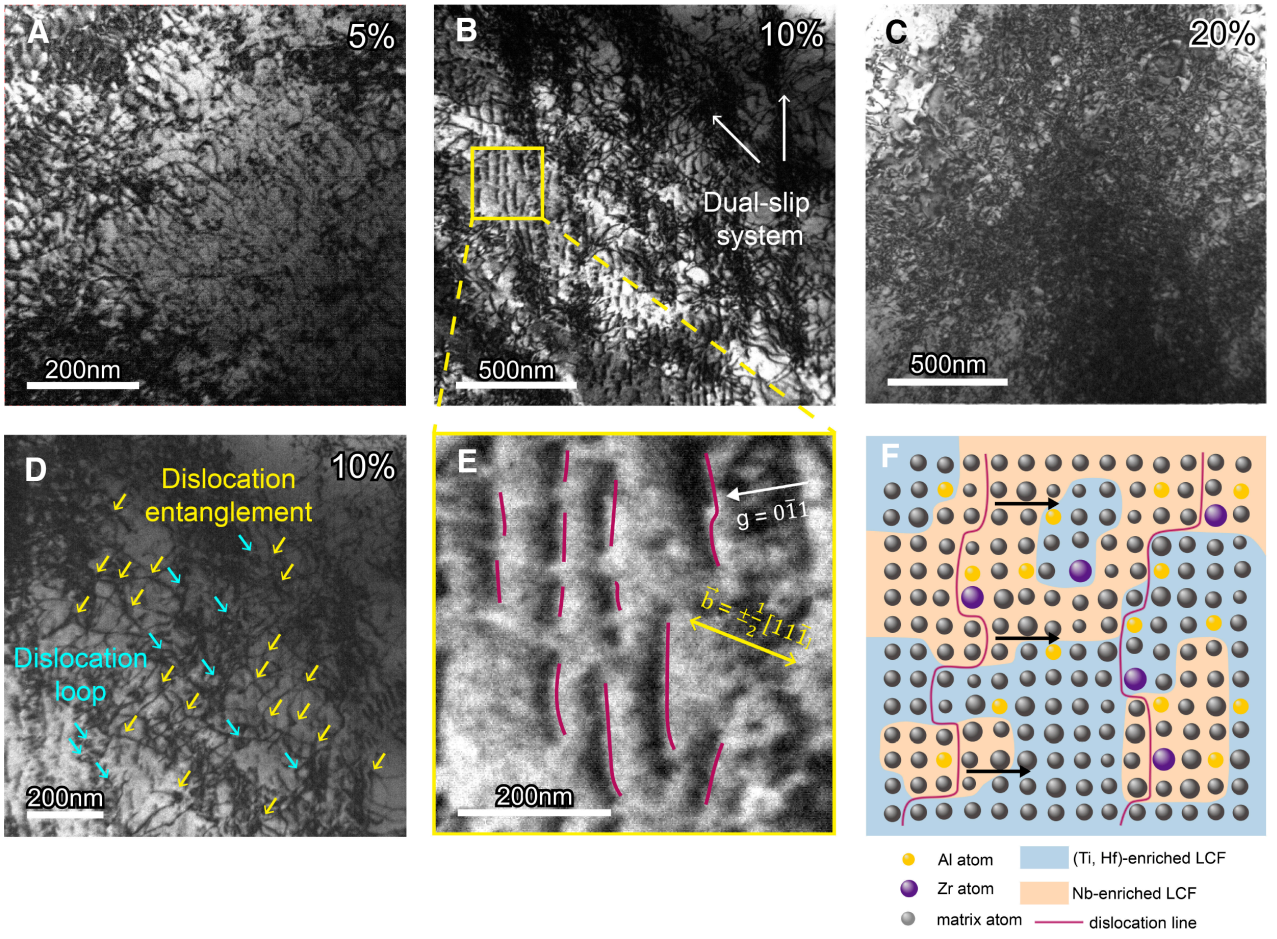

Fig. 4. Deformation mechanism of the Ti Sub 36 V Sub 14 Nb Sub 22 Hf Sub 22 Zr Sub 1 Al Sub 5 alloy. (*A*) A TEM image of the sample deformed to 5% strain, showing a high density of dislocations without localized slip-bands. The dislocation lines are smoothly curved, indicating a mixed character. (*B*) The dislocation morphology in a 10% strained sample. (*C*) A TEM image of the sample at a strain of 20%. Dislocations proliferate all over the deformed region. (*D*) A magnified TEM image of the 10% strained sample, showing the abundant dislocation entanglement points (yellow arrows) and dislocation loops (orange arrow). (*E*) A magnified image of the yellow square region in *B*. The dislocations lines are highlighted using violet lines. (*F*) Schematic illustration of the dislocation motion, which is retarded by the Zr/Al atoms with markedly different atomic radius with the matrix elements, and the ubiquitous Nb-enriched and Ti, Hf-enriched nanoscale fluctuations. All the TEM images here are taken under two-beam condition.

bands are very wide and dislocations also glide intensively in-between them. The abundant dislocation entanglements suggest strong dislocation interactions, and the dislocation loops (Fig. 4*D*) indicate dislocation multiplication through Frank-Read loops. Upon deformation, dislocations are frequently retarded by the ubiquitous ~1-nm-size Nb-enriched and (Ti, Hf)-enriched LCFs (Fig. 2*F*). The resultant sluggish motion and the wavy morphology of dislocations would increase their probability for running into one another, enhancing dislocation interaction and multiplication. With the enhanced tangling and looping of dislocations (Fig. 4*D*), the number density of sessile (immobile) dislocations increases, further elevating the slip resistance for dislocations. This promotes strain hardening and hence spreads out the plastic strain.

In bcc metals, the markedly higher velocity of edge dislocations compared to those of screw dislocations at ambient temperature leads to their rapid annihilation, resulting in the scarcity of observable edge dislocations in deformed bcc metals (42). Here, we note abundant edge dislocations with Burgers vector of $\pm\frac{1}{2}[11\bar{1}]$ (Fig. 4*E*). The dislocation types are determined according to the $\boldsymbol{g} \bullet \boldsymbol{b}$ extinction criterion (*SI Appendix*, Fig. S10). Fig. 4*E* was taken under $g = [0\bar{1}1]$ two-beam condition around the [111] zone axis. These short rod-like dislocations are always visible under $g = [0\bar{1}1]$ and $g = [\bar{1}\bar{1}0]$ two-beam conditions, while invisible under the $g = [101]$ two-beam conditions, suggesting that they are edge dislocations. The presence of abundant edge dislocations is notable, as regeneratable dislocation sources can be formed in bcc alloys through the coupled motion of edge and screw dislocations (40). This behavior is essential for the generation of a high density of dislocations along with straining. As such, at a strain of 20% (Fig. 4*C*), dislocations proliferate all over the deforming volume. The massive amounts of accumulated dislocations enhance strain hardening and strain delocalization.

To highlight the role played by the LCFs, another $Ti_{36}V_{14}Nb_{22}Hf_{22}Zr_1Al_5$ alloy was prepared using a higher cooling rate (cooled in liquid nitrogen instead of water, from 1,000 °C). A higher cooling rate is expected to lower the degree of LCF, rendering a state that is closer to a uniform solid solution (43). This alloy, for comparison, showed reduced uniform elongation and total tensile ductility (*SI Appendix*, Fig. S11). This suggests that the LCFs played a role in regulating dislocation patterns, making them markedly different from those in a random solid solution (20). These add spatially continuous but rugged energy landscapes that roughen dislocation lines and slow down their motion. Consequently, the MPEA not only shows a moderate increase in yield strength but also substantially increases chances for

dislocation interaction and multiplication, thereby increasing strain hardening and improving ductility. This effect is absent in conventional dilute solid solutions (5).

Through the development of the $Ti_{36}V_{14}Nb_{22}Hf_{22}Zr_1Al_5$ alloy, we show that a close-to-uniform MPEA solid solution—one that contains neither observable LCOs, nor 10-nm scale composition waves—can also reach strength–ductility combinations comparable to the best-performing bcc MPEAs thus far. This is, of course, mainly due to the large lattice distortion in this MPEA. In addition to lattice distortion, LCFs, LCOs and nanoprecipitates constituent different levels of chemical heterogeneities that help regulate moving dislocations (19). At the lowest level, 1-nm scale fully coherent LCFs originate from random statistical compositional fluctuations and remain fully coherent with the matrix; they retard dislocation motion and promote dislocation interactions (17); the LCF observed in our current RHEA could include a bit of undulation caused by LCO, but the chemical order should be slight such that it produces no diffraction signal or observable atomic planes enriched with certain elements under TEM. LCOs refer to partial chemical ordering over length scales from nearest-neighbor preference (chemical short-range order, SRO) to several-nanometer-sized domains (including complexes and spinodal modulations) (19). The effect of LCOs on strength depends on alloy chemistry—producing a minor impact in alloys with similar constituent elements (44) but significant strengthening in those containing vastly different species (e.g., solutes such as oxygen) (45). At the next level of chemical heterogeneity, phase separation introduces interphase interfaces that act as strong dislocation barriers, e.g., long-range ordered phases such as $L1_2$ nanoprecipitates (46) and eutectic systems containing $L2_1$ and bcc phases (47). Generally speaking, these three levels of chemical heterogeneities are expected to show increasing potency in strengthening and strain hardening. The present work answers the question as to what strength/ductility an essentially homogeneous solid solution can reach, when containing only LCFs but large lattice distortion.

In sum, we developed an ML-guided alloy design framework based on a physics-informed iterative learning loop. We demonstrated its predictability via realizing a large tensile ductility (42%) together with a gigapascal-level high yield strength in a bcc solid solution alloy. Such an AI-assisted strategy is expected to substantially accelerate the finding of high-performance alloys. It is especially useful for MPEAs with immense compositional space, in which alloys with desirable properties are difficult to locate in the vast unexplored composition space.

The $Ti_{36}V_{14}Nb_{22}Hf_{22}Zr_1Al_5$ solid solution alloy found in this work adopts a single-phase bcc structure, comprising alternating ~1-nm-sized Nb-enriched and (Ti, Hf)-enriched LCFs. The Zr/Al with markedly different atomic size and electronegativity from the other constituent elements increases lattice distortion, and the LCFs increase the difficulty for dislocation motion, contributing to the high yield strength. Furthermore, the ubiquitous LCFs substantially retard dislocation motion including nonscrew ones, and enable coordinated motion between edge and screw dislocations to promote regeneratable dislocation sources. This facilitates the continuous multiplication of dislocations all over the deformed region in lieu of narrow planar-slip bands, promoting strain hardening to suppress severe strain localization that risks early damage. Thus, the alloy achieves a very high tensile ductility even at gigapascal yield strength, which is uncommon in bcc solution alloys.

As a final note, the above-reported microstructure and property combination may be the extreme scenario one can reach, for MPEA solid solutions in this six-element system. It is an extreme in the sense that the alloy contains concentrated (including dissimilar) constituent elements and has developed LCFs, yet still remains a single-phase and nominally uniform solid solution with no dispersed LCOs, precipitates, and phase separation coming into the picture. These latter cases have been studied before in recent years under the name of MPEAs. They have achieved considerable success, although their design concepts are different from the original scope of high-entropy alloys, which were defined to be simple-structured (such as face-centered cubic and bcc) and homogeneous solid solutions. Many refractory high-entropy alloy systems have achieved outstanding properties through complex structural designs (e.g., B2-like LCOs and long-range orders), expanding the traditional scope of high-entropy alloys. In this paper, we show the best scenario/property that can be managed if one stays with a solid solution that is within the original scope of HEAs. How far the HEAs can take us to, in terms of microstructure and strength–ductility, is answered here by the $Ti_{36}V_{14}Nb_{22}Hf_{22}Zr_1Al_5$ bcc solid solution for this senary alloy system.

Materials and Methods

Material Preparation. The compositions and heat treatment parameters for all alloy specimens were determined through iterative machine learning (ML) optimization. The $Ti_{36}V_{14}Nb_{22}Hf_{22}Zr_1Al_5$ alloy and its base alloy $Ti_{38}V_{15}Nb_{23}Hf_{24}$ were fabricated using high-purity Ti, V, Nb, Hf, Zr, and Al (more than 99.95 wt%) by vacuum arc melting in a Ti-gettered argon atmosphere. Ingots were remelted at least 10 times to ensure the initial chemical homogeneity. The as-cast ingots were cut into 5-mm-thickness plates by an electric discharge machine. According to the results of ML iterations, the plates were cold-rolled to a thickness reduction of roughly 80% to 1 mm and then annealed at 1,000 °C for 5 min under an Ar atmosphere, followed by water quenching.

Measurements of Mechanical Properties. Room-temperature tensile tests were performed under CMT4304 testing machine at a strain rate of 5×10^{-4} s^{-1}. Dog-bone-shaped sample with a cross-section of 1×2 mm^2 and a gauge length of 6 mm were cut from the rolled and annealed plate by electric discharge machine.

Microstructural Analysis. XRD tests of the $Ti_{36}V_{14}Nb_{22}Hf_{22}Zr_1Al_5$ alloy and its base alloy $Ti_{38}V_{15}Nb_{23}Hf_{24}$ were carried out using a Cu-Kα radiation source, scanned in the 2θ range of 10 to 100° at a speed of 0.2° s^{-1}. Before XRD scanning, the samples were polished with 600 and 1,000-grit SiC papers. EBSD analysis were all performed in a ZEISS Gemini SEM 500 field-emission scanning electron microscope. Specimens for EBSD investigation were polished to achieve mirror-finish surface conditions.

TEM samples are mechanically ground to a thickness of about 25 μm, followed by ion-polished to a thickness of about 10 μm with an EM RES102 ion milling system. The dislocations of deformed $Ti_{36}V_{14}Nb_{22}Hf_{22}Zr_1Al_5$ samples were analyzed using a JEM-2100 TEM. HAADF–STEM and EDS mapping was performed at JEM-ARM300F2 double aberration-corrected scanning transmission electron microscope (STEM) operated at 300 kV. The elemental line profiles are smoothed with a Savitzky–Golay filter using a 30-point window and 2nd-order polynomial. The corresponding strain maps were obtained by using the GPA method (48). The fracture surface was analyzed using the SEM 4000 Thermal field scanning electron microscope.

Data, Materials, and Software Availability. The machine learning code and data have been deposited in GitHub (https://github.com/Xiangyue-Chen/Active-learning-design-of-bcc-solid-solution-alloys) (49). Other data are included in the article and/or *SI Appendix*.

ACKNOWLEDGMENTS. We acknowledge the supports from the National Natural Science Foundation of China [Grant No. 52371162 (C.L.), 52231001 (E.M.), 52361165617 (G.W.), 52271114 (G.W.), 52127801 (X.Z.), 52425101 (X.Z.), 52401216 (Z.R.)], open research fund of Suzhou Laboratory (No. SZLAB-1108-2024-TS001), Key Technologies R&D Program (Grant Nos. 2024YFB3817600), and Fundamental and Interdisciplinary Disciplines Breakthrough Plan of the Ministry of Education of China, (Grant Nos. JYB2025XDXM411). G.W., Z.R., and C.L. also acknowledge the support from the National Natural Science Fund for

Excellent Young Scientists Fund Program (Overseas). We are grateful for the technical support from Chuansheng Ma, Peng Zhang, Yuanbin Qin, Pengcheng Zhang, Qinqin Fu, Chaowei Guo, Chuanwei Fan, and Danli Zhang at Xi'an Jiaotong University. We thank Dr. Chuansheng Ma and Dr. Zijun Ren, at Instrument Analysis Center of Xi'an Jiaotong University for their assistance with electron microscopy characterization.

1. G. Gottstein, *Physical Foundations of Materials Science* (Springer, 2016), pp. 264–274.
2. P. J. Yang, Q. J. Li, W. Z. Han, J. Li, E. Ma, Designing solid solution hardening to retain uniform ductility while quadrupling yield strength. *Acta Mater.* **179**, 107–118 (2019).
3. Y. Wang *et al.*, Strength-ductility trade-off in NbTaxTiV refractory multi-principal element alloys. *Mater. Sci. Eng. A* **922**, 147677 (2025).
4. Y. Wu *et al.*, Relationship between the unique microstructures and behaviors of high-entropy alloys. *Int. J. Miner. Metall. Mater.* **31**, 1350–1363 (2024).
5. L. Wang *et al.*, Tailoring planar slip to achieve pure metal-like ductility in body-centred-cubic multi-principal element alloys. *Nat. Mater.* **22**, 950–957 (2023).
6. Z. An *et al.*, Negative mixing enthalpy solid solutions deliver high strength and ductility. *Nature* **625**, 697–702 (2024).
7. G. L. W. Hart, T. Mueller, C. Toher, S. Curtarolo, Machine learning for alloys. *Nat. Rev. Mater.* **6**, 730–755 (2021).
8. X. Liu, J. Zhang, Z. Pei, Machine learning for high-entropy alloys: Progress, challenges and opportunities. *Prog. Mater. Sci.* **131**, 101018 (2023).
9. X. Huang, L. Zheng, H. Xu, H. Fu, Predicting and understanding the ductility of BCC high entropy alloys via knowledge-integrated machine learning. *Mater. Des.* **239**, 112797 (2024).
10. C. Lee *et al.*, Lattice distortion enhanced yield strength in a refractory high-entropy alloy. *Adv. Mater.* **32**, 2004029 (2020).
11. Z. An *et al.*, A novel HfNbTaTiV high-entropy alloy of superior mechanical properties designed on the principle of maximum lattice distortion. *J. Mater. Sci. Technol.* **79**, 109–117 (2021).
12. S. Guo, C. T. Liu, Phase stability in high entropy alloys: Formation of solid-solution phase or amorphous phase. *Prog. Nat. Sci. Mater. Int.* **21**, 433–446 (2011).
13. Y. Zhang *et al.*, Novel BCC Ti-Al-Nb-Zr medium-entropy alloys with ultrahigh specific strength and ductility. *J. Alloys Compd.* **936**, 168290 (2023).
14. O. N. Senkov, S. V. Senkova, C. Woodward, D. B. Miracle, Low-density, refractory multi-principal element alloys of the Cr-Nb-Ti-V-Zr system: Microstructure and phase analysis. *Acta Mater.* **61**, 1545–1557 (2013).
15. Q. Ding *et al.*, Tuning element distribution, structure and properties by composition in high-entropy alloys. *Nature* **574**, 223–227 (2019).
16. A. Takeuchi, A. Inoue, Classification of bulk metallic glasses by atomic size difference, heat of mixing and period of constituent elements and its application to characterization of the main alloying element. *Mater. Trans.* **46**, 2817–2829 (2005).
17. Y. Bu *et al.*, Local chemical fluctuation mediated ductility in body-centered-cubic high-entropy alloys. *Mater. Today* **46**, 28–34 (2021).
18. M. Zhang, B. Zhang, J. Ding, E. Ma, Quantifying the local compositional fluctuation and Shannon entropy inherent in multi-principal element alloys. *Scr. Mater.* **259**, 116559 (2025).
19. E. Ma, J. Ding, Compositional fluctuation and local chemical ordering in multi-principal element alloys. *J. Mater. Sci. Technol.* **220**, 233–244 (2025).
20. Q.-J. Li, H. Sheng, E. Ma, Strengthening in multi-principal element alloys with local-chemical-order roughened dislocation pathways. *Nat. Commun.* **10**, 3563 (2019).
21. J. Qi *et al.*, Integrated design of aluminum-enriched high-entropy refractory B2 alloys with synergy of high strength and ductility. *Sci. Adv.* **10**, 49 (2024).
22. Y. Li *et al.*, Machine learning-assisted design of Ti–V–Nb–Mo refractory high-entropy alloys with higher ductility and specific yield strength. *J. Mater. Res. Technol.* **34**, 1732–1743 (2025).
23. W. Huang, J. Hou, X. Wang, J. Qiao, Y. Wu, Excellent room-temperature tensile ductility in as-cast Ti37V15Nb22Hf23W3 refractory high entropy alloys. *Intermetallics* **151**, 107735 (2022).
24. Y. Zhou *et al.*, Strategies for optimizing mechanical properties of refractory high entropy alloys induced by solid solution strengthening mechanism. *Mater. Sci. Eng. A.* **923**, 147696 (2025).
25. M. Akmal, H. W. Seong, H. J. Ryu, Mo and Ta addition in NbTiZr medium entropy alloy to overcome tensile yield strength-ductility trade-off. *J. Mater. Sci. Technol.* **109**, 176–185 (2022).
26. Y. Chen *et al.*, Microstructure and mechanical properties of TiNbV0.5Ta0.5Crx (x=0, 0.1, 0.2, 0.5) refractory high-entropy alloys. *J. Mater. Sci. Technol.* **211**, 254–266 (2025).
27. S. Zeng *et al.*, Microstructure and mechanical properties of lightweight Ti3Zr1.5NbVAlx (x = 0, 0.25, 0.5 and 0.75) refractory complex concentrated alloys. *J. Mater. Sci. Technol.* **130**, 64–74 (2022).
28. J. Qin *et al.*, Microstructure, mechanical properties and incipient plasticity of (Ti42.5Zr42.5Nb10Ta5)100-xMox refractory high-entropy alloys. *J. Mater. Res. Technol.* **30**, 8128–8136 (2024).
29. Y. Wang *et al.*, Hf-induced strengthening and lattice distortion in HfxNbTaTiV refractory multi-principal element alloys. *J. Mater. Res. Technol.* **34**, 2527–2538 (2025).
30. J. Wang *et al.*, Synergistic effects of Hf and Ta on strength-ductility in refractory high-entropy alloys: Kink band formation and dislocation evolution. *Acta Mater.* **300**, 121492 (2025).
31. W. Lai *et al.*, Design of BCC refractory multi-principal element alloys with superior mechanical properties. *Mater. Res. Lett.* **10**, 133–140 (2022).
32. X. Yan, Y. Zhang, A body-centered cubic Zr50Ti35Nb15 medium-entropy alloy with unique properties. *Scr. Mater.* **178**, 329–333 (2020).
33. Y. Luo *et al.*, Novel as-cast HfNbTaTiAl refractory multi-principal element alloys with superior strength-ductility combination at room temperature. *Mater. Sci. Eng. A.* **916**, 147375 (2024).
34. J. Gong *et al.*, A single-phase Nb25Ti35V5Zr35 refractory high-entropy alloy with excellent strength-ductility synergy. *J. Alloys Compd.* **1006**, 176290 (2024).
35. E. Ma, C. Liu, Chemical inhomogeneities in high-entropy alloys help mitigate the strength–ductility trade-off. *Prog. Mater. Sci.* **143**, 101252 (2024).
36. J. Pang *et al.*, Simultaneous enhancement of strength and ductility of body-centered cubic TiZrNb multi-principal element alloys via boron-doping. *J. Mater. Sci. Technol.* **78**, 74–80 (2021).
37. Z. An *et al.*, Spinodal-modulated solid solution delivers a strong and ductile refractory high-entropy alloy. *Mater. Horiz.* **8**, 948–955 (2021).
38. L. Lilensten *et al.*, Study of a bcc multi-principal element alloy: Tensile and simple shear properties and underlying deformation mechanisms. *Acta Mater.* **142**, 131–141 (2018).
39. B. Chen *et al.*, Correlating dislocation mobility with local lattice distortion in refractory multi-principal element alloys. *Scr. Mater.* **222**, 115048 (2023).
40. Y. Lu, Y. H. Zhang, E. Ma, W. Z. Han, Relative mobility of screw versus edge dislocations controls the ductile-to-brittle transition in metals. *Proc. Natl. Acad. Sci. U.S.A.* **118**, 37 (2021).
41. F. Wang *et al.*, Multiplicity of dislocation pathways in a refractory multiprincipal element alloy. *Science* **370**, 95–101 (2020).
42. B. Chen *et al.*, Unusual activated processes controlling dislocation motion in body-centered-cubic high-entropy alloys. *Proc. Natl. Acad. Sci. U.S.A.* **117**, 16199–161206 (2020).
43. T. Li *et al.*, CALPHAD-aided design for superior thermal stability and mechanical behavior in a TiZrHfNb refractory high-entropy alloy. *Acta Mater.* **246**, 118728 (2023).
44. B. Yin, S. Yoshida, N. Tsuji, W. A. Curtin, Yield strength and misfit volumes of NiCoCr and implications for short-range-order. *Nat. Commun.* **11**, 2507 (2020).
45. Z. He *et al.*, Interstitial-driven local chemical order enables ultrastrong face-centered cubic multicomponent alloys. *Acta Mater.* **243**, 118495 (2023).
46. S. Zhao *et al.*, Negative mixing enthalpy route guides strong and ductile soft magnetic high-entropy alloys with high saturation magnetization. *Mater. Today* **88**, 45–54 (2025).
47. M. Wang *et al.*, Lightweight, ultrastrong and high thermal-stable eutectic high-entropy alloys for elevated-temperature applications. *Acta Mater.* **248**, 118806 (2023).
48. M. J. Hÿtch, E. Snoeck, R. Kilaas, Quantitative measurement of displacement and strain fields from HREM micrographs. *Ultramicroscopy* **74**, 131–146 (1998).
49. X. Y. Chen, Active learning design of bcc solid solution alloys. GitHub. https://github.com/Xiangyue-Chen/Active-learning-design-of-bcc-solid-solution-alloys. Deposited 30 December 2025.